Optically transparent ultrathin NiCo alloy oxide film: Precise oxygen vacancy modulation and control for enhanced electrocatalysis of water oxidation

Xue Yu [a,1], Chengwei Hu [a,1], Peixuan Ji [a], Yanmei Ren [a], Hongyuan Zhao [a], Gen Liu [a], Rui Xu [a], Xiaodong Zhu [a], Zhiqing Li [c], Yanqing Ma [a,b,*], Lei Ma [a,**]

[a] Tianjin International Center for Nanoparticles and Nanosystems, Tianjin University, Tianjin 300072, PR China
[b] State Key Laboratory of Precision Measuring Technology and Instruments, Tianjin University, Tianjin 300072, PR China
[c] Tianjin Key Laboratory of Low Dimensional Materials Physics and Preparing Technology, Department of Physics, Tianjin University, Tianjin 300072, PR China

ARTICLE INFO

ABSTRACT

Oxygen evolution reaction (OER) impedes the electrochemical water splitting for H_2 production primarily because of the sluggish kinetics. Cobalt oxides with abundant oxygen vacancies (Vos) have been proved to be the promising OER electrocatalysts showing high catalytic performance. However, precisely controlling the concentration of the Vos and large-scale synthesis of these electrocatalysts are still not resolved. Herein, we propose an e-beam evaporation alloy-UV/O_3 oxidation method for fabricating optically transparent alloy oxide films (f-$Ni_{0.1}Co_{0.9}O_x$) only 10 nm thick. The concentration of the oxygen vacancies is positive correlated with the Ni content in the alloy oxides. The optimum binary Ni/Co (1/9) alloy oxide with the best defect O/lattice O ratio (0.952) exhibits ultrahigh OER mass activity of 3055 A g^{-1} at 250 mV overpotential in 1.0 M KOH, almost 7.5 times and 190 times as high as CoO_x and the commercial benchmark RuO_2 OER catalysts, respectively. Moreover, directly depositing f-$Ni_{0.1}Co_{0.9}O_x$ film on the top of the tandem-junction a-Si PV cell realizes wireless unassisted solar-driven water splitting with high solar-to-hydrogen conversion efficiency. The key roles of modulating the electron structure, stably reversible spinel structure and the reaction barrier reduction were revealed in situ spectroscopy and density functional theory calculations. This study provides a new perspective of oxygen vacancy modulation for high electrocatalysis performance via large-scale synthesis of such bimetallic alloy oxides.

1. Introduction

Hydrogen is an ideal energy carrier in the sustainable energy supply system. Oxygen evolution reaction (OER) is a major bottleneck in the energy conversion technique of solar and electricity to hydrogen, such as water electrocatalysis and water photoelectrocatalysis, owing to its requirement of a large overpotential in its complex four-electron transfer process [1–4]. A number of noble metal catalysts such as Ir/C, IrO_2 and RuO_2 have been intensively investigated due to their excellent OER performance, however, their high cost and scarcity inhibit the long-term application [5–7]. In recent decades, transition metal oxides (TMOs) have been considered as the best potential alternatives due to their abundance, cost-effectiveness and stability [8–11]. Especially, the

cobalt-based oxides (Co_3O_4, CoO, CoOOH, CoO_x etc.) synthesized by hydrothermal or electrodeposition chemical methods, have demonstrated relatively high OER electrocatalytic activities [12–16]. However, complex preparation process and high production cost of traditional chemical synthetic methods limit their practical industrial-scale application. Therefore, developing a simple, and scalable technique is still pressingly needed for practical applying TMOs OER electrocatalyst [17, 18]. It has been extensively reported the defect engineering enhanced the OER activity such as applying oxygen vacancy (Vo) to cobalt oxides [19–22]. Compared with crystalline TMOs, defective oxides have flexible disordered lattice structure, which tends to increase the catalytic active sites and facilitates electron transfer [23–25]. With the help of oxygen vacancies (Vos), the surface atomic arrangement and electron

---

structure of the oxides can be modulated to improve the electrical conductivity and reaction rate. The Vos are also found to activate surrounding atoms to increase the reactivity of active sites [26–28]. In the past decade, there are many reports on improving OER performance through oxygen defects on the surface of cobalt oxides made by chemical reduction or plasma etching [23,29–31]. However, random distribution and excessive amount of Vos would make their structure unstable and even have side effects on the catalytic reaction [19]. A recent noticeable and efficient way for introducing oxygen vacancy is lowering coordination atoms of the surficial Co sites by introducing heteroatoms or compounds (eg. Fe [32], Ni [33], NiO [34]). The introduction of hybrids in CoO_x can expand the potential range of thermodynamic metastability to provide a stable oxide structure as substrate for the growth of the active species under OER condition [32]. The lower coordination atoms (LCAs) can modulate the electronic structure between them and their neighboring atoms, which is in favor of optimal adsorption energies for intermediates [34]. In addition, the homogeneous heteroatomic mixing in CoO_x structure ensure the surficial uniform distribution of active sites [35]. Especially, different oxidation states from the mixed oxides can facilitate a large number of defects such as Vos formation on the surface [34,36]. However, the structure-activity relation between the concentration of the surficial Vos and electrocatalytic activity of the Co-based oxides with LCAs has not yet been reported systematically to our knowledge.

Herein, we demonstrate a strategy for optimizing surficial oxygen vacancy concentration by introducing heteroatom Ni in the CoO_x to form bimetallic alloy oxide. We use the e-beam evaporation alloy-UV/O_3 oxidation without any extreme chemical environment, such as high temperature and pressure, to realize large-scale synthesis of the optically transparent spinel NiCo alloy oxide film (f-$Ni_{0.1}Co_{0.9}O_x$). The obtained ultrathin f-$Ni_{0.1}Co_{0.9}O_x$ film only 10 nm thick consists of nano-islands with an average size of about 35 nm. X-ray photoelectron spectroscopy (XPS) data verifies that the ratios of Co^{2+}/Co^{3+} and OII/OI (defect O/lattice O) increase with the increase of Ni content. The operando Raman spectroscopy demonstrates a reversible spinel structure and a faster amorphous reconstruction for alloy oxide prior to the OER process. Other experimental and theoretical calculations confirm that the surficial oxygen vacancies of f-$Ni_{0.1}Co_{0.9}O_x$ not only could provide more active sites, tailor electronic structure but also reduce the energy barrier of the intermediate formation. With the accurate control of the oxygen vacancy concentration, the f-$Ni_{0.1}Co_{0.9}O_x$ serves as an excellent catalyst for OER with ultrahigh catalytic mass activity about 3055 A g^{-1} at 250 mV overpotential, yielding mass activity almost 190 times and 7.5 times higher than that of commercial RuO_2 and as-prepared CoO_x, respectively. Additionally, the f-$Ni_{0.1}Co_{0.9}O_x$ is applied to deposit on tandem-junction a-Si solar cell to construct an unassisted wireless integrated photoelectrical water splitting system, which reaches a solar-to-hydrogen (STH) conversion efficiency of 11%. This work opens a door for the electrocatalyst investigation of other binary or multiple alloy oxide with controlled oxygen vacancies towards energy storage and photoelectrochemical conversion applications.

2. Experimental section

All the chemicals were used as received without further purification unless otherwise specified.

2.1. Synthesis of NiCo alloy oxide film (f-Ni₀.₁Co₀.₉Oₓ)

The f-$Ni_{0.1}Co_{0.9}O_x$ was prepared by e-beam evaporation method followed by ultraviolet lamp irradiation with O_2 gas flowing. The details are as follows. All the electrodes were prepared on ITO substrates (Indium tin oxide, 250 nm thickness on the glass, 5 Ω cm^{-2} resistance) and ITO/ tandem-junction a-Si (3j-a-Si, Xunlight Corp.) photovoltaic films. Typically, before deposition, the Co target (99.99%, 1.805 g) and Ni target (99.99%, 0.203 g) were washed with ethanol and deionized water

for few times to remove the impurities. Deposition was performed in SAIS (Shenyang Academy of Instrumentation Science) electron-beam (E-beam) evaporation instrument with a base pressure of 4.0 × 10^{-4} Pa. The electron-beam bombarded the Co target and Ni target until metals were mixed and interfused for 30 min. Then, the total deposited sample thickness (10 nm) was monitored via a quartz crystal with a targeted deposition rate of 0.1 Å s^{-1} for Ni/Co alloy (about 1/9 molar ratio). After that, the alloy/ITO glass and alloy/ITO/3j-a-Si were transferred into the oxidation cavity, and calcined at 160 ℃ for 30 min with a O_2 flow rate of 200 sccm (standard-state cubic centimeter per minute) under UV light irradiation (30 mW cm^{-2}) for oxidation. Finally, the Ni/Co alloy oxide (named as f-$Ni_{0.1}Co_{0.9}O_x$) was obtained by cooling down to room temperature with natural cooling process under a N_2 flow rate of about 30 sccm. The as-obtained f-$Ni_{0.1}Co_{0.9}O_x$/ITO was directly used as working electrode without further loading process. Other Ni/Co alloy-oxides were prepared using the same method as f-$Ni_{0.1}Co_{0.9}O_x$ just altering different Ni contents in Ni/Co alloy (about 5% and 30%, molar percentage), named as f-$Ni_{0.05}Co_{0.95}O_x$ and f-$Ni_{0.3}Co_{0.7}O_x$, respectively.

2.2. Synthesis of Co oxides (f-CoOₓ) and Ni oxides (f-NiOₓ)

The f-CoO_x sample was synthesized using the same method as f-$Ni_{0.1}Co_{0.9}O_x$ just removing the Ni target. The f-NiO_x sample was synthesized using the same method as f-$Ni_{0.1}Co_{0.9}O_x$ just removing the Co target.

2.3. Characterization

Surface morphology of samples were characterized by atomic force microscope (AFM, Park NX10), scanning electron microscope (SEM, Hitachi, SU-3500) and scanning tunneling microscope (STM, FM-NanoviewT). Energy dispersive X-ray spectroscopy (EDS, IXRF SYSTEM, SU-3500) was used to characterize the type of the elements and elemental distribution. The Raman spectra and operando Raman spectra used Raman spectrometer (ANDOR-MARZHAUSER) with a 785 nm laser and the power was about 2 mW at the objective. The X-ray photoelectron spectroscopy (XPS, Thermo Scientific, ESCALAB 250Xi) was used to analyze surficial structural information. XPS binding energies were reported referenced to the C 1 s line at 284.6 eV banding energy for adventitious carbon. UV–vis absorption spectrum and the operando UV–vis absorption spectrum were taken on a Hitachi U-3900 UV–vis spectrometer. Inductively coupled plasma-mass spectrometry (ICP-MS, Agilent 7700X) was used to test the mass of the metal content in the alloy oxide. Electrostatic force microscopy (EFM, Park NX10) was used to observe the electrostatic voltage to analyze the conductivity of the material. The electron spin resonance spectroscopy (ESR, JEOL, JES-FA200) was used to test signal of the electron trapping at oxygen vacancy.

2.4. DFT calculations

all density functional theory calculations were performed by Vienna Ab initio Simulation Package (VASP) with projector augmented wave (PAW) method and the PBE generalized gradient approximation (GGA) exchange correlation function. For the plane-wave basis set, the kinetic energy cutoff was set to 500 eV. Brillouin zone integration was sampled with the 3 × 2 × 1grid of k-point and 16 × 12 × 1 grid of k-point for the density of states (DOS), respectively. Considering the strong correlation effects intransition metals, electronic structure calculations and structural relaxations were performed using a spin-dependent GGA plus Hubbard U method. Ueff (U – J) = 3.52 eV for Co 3d states and 3.00 eV for Ni 3d states. were adopted, respectively. The model of Co_3O_4 (110) surface was constructed based on the vacuum layer of 20 Å. The O vacancy was construct by removing one oxygen atom during the structural optimization process. The Ni atom was located at Co_3O_4 (110) surface. The energy convergence tolerance of 10^{-4} eV per atom and the final

force on each atom of 0.03 eV Å^{-1} were adopted. The Gibbs free energies and other details were calculated in the supporting information.

3. Results and discussion

3.1. Catalyst synthesis and morphology characterization

The simple two-step process of f-Ni$_{0.1}$Co$_{0.9}$O$_x$ involves alloy evaporation and oxidation as illustrated in Fig. 1a. First, the Ni/Co alloy clusters evaporate via electron-beam bombardment and deposit on ITO glass substrate to form alloy nano-islands with average size of about 15 nm (Fig. S1, Supporting Information). Then, the NiCo alloy layer is oxidized by UV-Ozone treatment at 160 ℃, thus forming alloy oxide nano-islands with average size of about 35 nm showed in atomic force microscope (AFM) image and atmospheric pressure scanning tunnelling microscope (STM) from Fig. 1b-d. UV-Ozone treatment as a photosensitized oxidation process, can generate activated oxygen (O*) and ozone to react with NiCo alloy to produce alloy oxides [37]. The STM images of the oxide films with different content of Ni are provided in Fig. S2. It can be observed the nano-islands of alloy oxides almost have the average size of 35 nm without obvious difference for different Ni/Co ratios. However, the Ni content increasing in the NiCo oxide, the surface of the nano-island contains more small particles (Fig. S3). This small size and surficial particles are in favor for much exposed surface/edge defects, which can be formed as the active sites at the interface or on the surface [19]. The energy-dispersive X-ray spectrometer (EDS) mapping images evidence the uniform distribution of elements Ni, Co and O of the binary alloy oxide f-Ni$_{0.1}$Co$_{0.9}$O$_x$ (Fig. 1e). In addition, the atom ratio of Ni/Co is determined to be 0.11/0.89 on the surface by X-ray photoelectron spectroscopy (XPS) almost associated with the bulk contents detected by the EDS spectroscopy (Table S1 and Fig. S4) [38]. Moreover, comparing with the transmittance of ITO substrate, only less than 10% light absorption from 450 nm to 800 nm indicates the great optical transparent property of f-Ni$_{0.1}$Co$_{0.9}$O$_x$ film in Fig. 1f. The thickness of this ultrathin film is less than 10 nm (Fig. S5). This advantage of optical transparency greatly contributes to the integrated electrocatalyst-solar cell device application [39].

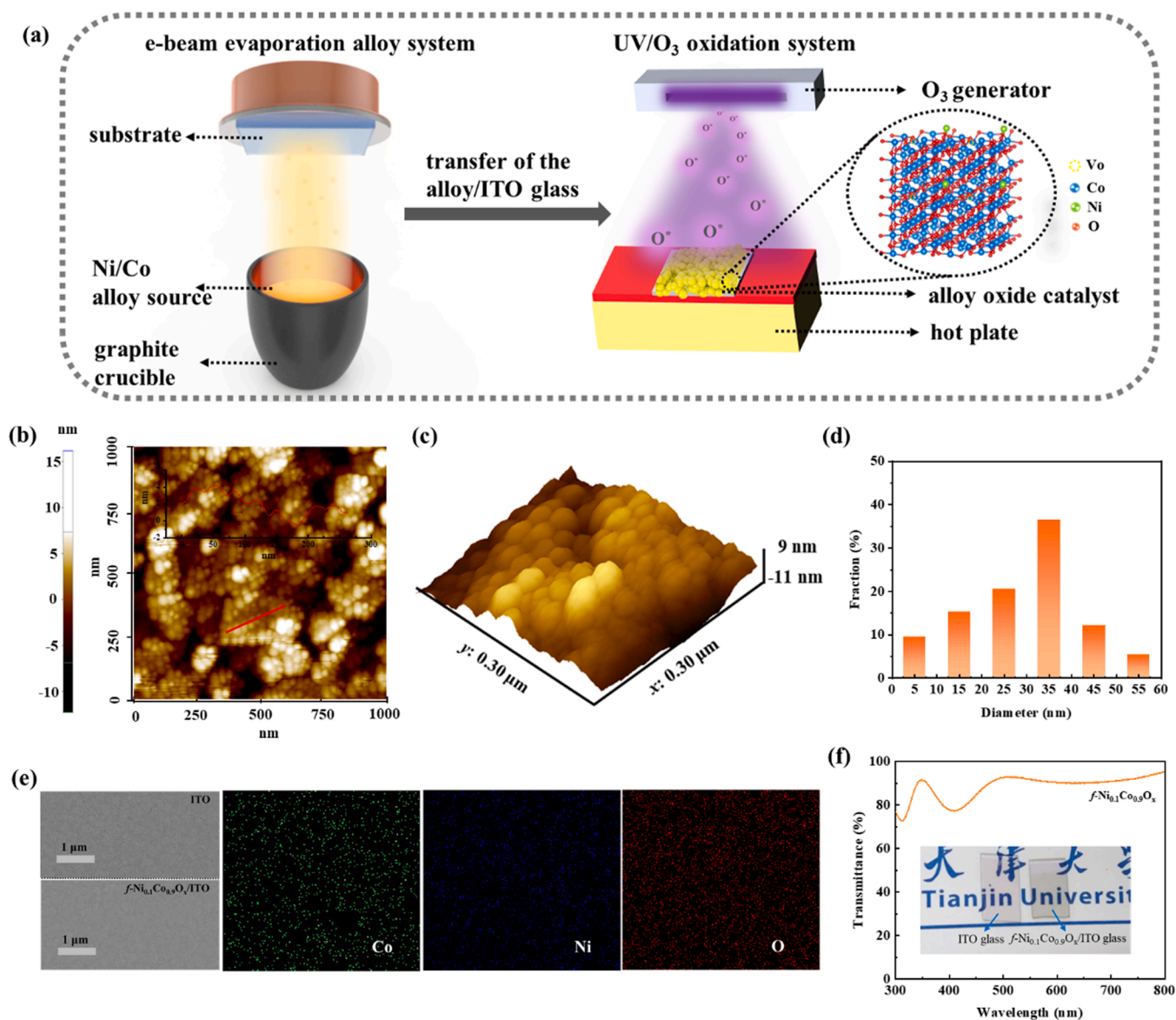**Fig. 1.** (a) Schematic illustration of the synthetic process of f-Ni$_{0.1}$Co$_{0.9}$O$_x$ film. (b) AFM image, (c) three-dimensional STM image and (d) the corresponding diameter histogram of the nano-island of f-Ni$_{0.1}$Co$_{0.9}$O$_x$. (e) SEM of ITO and f-Ni$_{0.1}$Co$_{0.9}$O$_x$ /ITO and EDS mapping images of f-Ni$_{0.1}$Co$_{0.9}$O$_x$ /ITO. (f) UV–vis absorption spectrum and photograph of f-Ni$_{0.1}$Co$_{0.9}$O$_x$.

3.2. Composition, value state and oxygen vacancy analysis of f-$Ni_{0.1}Co_{0.9}O_x$

Close observation of composition and crystalline phases can be seen from the X-ray diffraction patterns (XRD) as shown in Fig. S6. The peaks of samples deposited on ITO glass substrates difficultly avoid the strong impact of ITO peaks. The weak pattern of the pristine f-CoO_x matches with a typical spinel Co_3O_4 structure (JCPDS No. 43–1003) [26]. In the case of f-$Ni_{0.1}Co_{0.9}O_x$, the XRD pattern keeps unchanged with no apparent diffraction peaks corresponding to NiO_x, and the peaks corresponding to spinel Co_3O_4 become weaker, indicating the existence of the amorphous phase or crystalline phase but with a very small size for NiO_x [40,41]. To further clarify the detailed local crystal structure, Raman spectroscopy is used to investigate under dry condition as shown in Fig. 2a. It is illustrated that the sharp and intense peaks located at 190, 479, 521, 613, and 689 cm^{-1} are in agreement with 3 F_{2g}, $1E_g$, and $1A_{1g}$ Raman-active modes of the spinel structure for Co_3O_4 crystal in the exposed f-CoO_x [42]. It is worth noting that the various vibration modes in the Raman spectra of NiCo alloy oxides become attenuated and broaden when increasing Ni content of alloy. This result suggests that increasing Ni incorporation leads to the crystallite size toward small growth even amorphourization [43,44]. Notably, compared with f-CoO_x, increasing the Ni contents facilitates the Raman peaks of alloy oxides shift to low wavenumber direction, suggesting increase of Vos [44,45].

Analyzing the surface oxidation states of NiCo alloy oxide is of importance to investigate the existence of oxygen vacancy. The X-ray photoelectron spectra (XPS) of f-CoO_x, f-$Ni_{0.05}Co_{0.95}O_x$, f-$Ni_{0.1}Co_{0.9}O_x$ and f-$Ni_{0.3}Co_{0.7}O_x$ are shown in Fig. 2b-d. In the Co 2p region, the f-$Ni_{0.1}Co_{0.9}O_x$ shows the major peaks with binding energy of 796.4 eV and 780.5 eV, attributing to the $2p_{1/2}$ and $2p_{3/2}$, respectively (Fig. S7) [46]. An approximate 15 eV energy variation between the $2p_{1/2}$ and $2p_{3/2}$ suggests the coexistence of Co^{3+} and Co^{2+} species [47]. In the Co $2p_{3/2}$ spectra, peaks features at 779.7 eV and 781.2 eV, assigning to Co^{3+} and Co^{2+} cations, respectively (Fig. 2b) [48]. As such, the relative area ratio of Co^{2+}/Co^{3+} for f-$Ni_{0.1}Co_{0.9}O_x$ (≈ 0.547) is higher than that of f-CoO_x (≈ 0.265), indicating that the embedded nickel atoms influence more

Co^{2+} formed on the surface [45]. As further observed, increasing Ni content contributes to much appearance of low oxidation state (Co^{2+}), as compared to pure f-CoO_x. This result infers that Ni in the alloy oxide can reduce the coordination numbers of the neighbored Co-O, thus influencing the electron structure of the catalyst, further changing the absorption property of active species [49]. The O1s spectra of the above four samples are appropriately analyzed according to the following details (Fig. 2c). OI peaks are corresponding to the lattice oxygen species from Co oxide and Ni oxide. The peak at 529.6 eV is attributed to lattice O from Co oxide. The peaks at 530.1 eV and 531.7 eV are attributed to lattice O from Ni^{2+} oxide and Ni^{3+} oxide, respectively [37]. OII located at 531.2 eV is indexed to oxygen vacancy in the lattice and OIII located at 532.6 eV originates from adsorbed oxygen in water molecule [48]. It can be found that the OII peak appears in all above samples, implying the introducing of the oxygen vacancies on the surface of the catalysts. By the comparison of the O1s spectra in different NiCo alloy oxides, the ratio of OII/OI apparently increases when increasing the Ni content as shown in Fig. 2c and d. It suggests that Ni oxidation reaction influence Co oxidation process, resulting in incomplete oxidation for cobalt oxide, thus much oxygen vacancies appearing. Moreover, the same tendency is that the ratio Ni^{2+}/Ni^{3+} is also increased when Ni content increased, further demonstrating the incomplete oxidation of the bimetal oxides (Fig. S8). Additionally, the oxygen vacancies are further demonstrated by room-temperature electron spin resonance (ESR) spectroscopy as shown in Fig. S9. It is obviously found that the ESR signal at g= 2.003 (electron trapping at oxygen vacancy) [17,50] become stronger with the increase of the Ni content in the metal oxides. This result indicates abundant oxygen vacancies can be produced when increasing Ni in the NiCo alloy oxides, which is consistent with the result of XPS analysis. On the basis of above, it can be concluded that lower coordination numbers of Co atoms and more oxygen vacancies co-exist on the surface of catalyst by precisely modulating the Ni/Co ratio of the alloy oxide [45, 51–53]. In addition, the UV/O_3 oxidation process also can cause oxygen vacancies as demonstrated by XPS and ESR results of pure f-CoO_x. The UV/O_3 oxidation process for oxygen vacancy will not be here discussed excessively because the same oxidation treatment including O_2, temperature and oxidation time is used for both f-CoO_x and other NiCo alloy
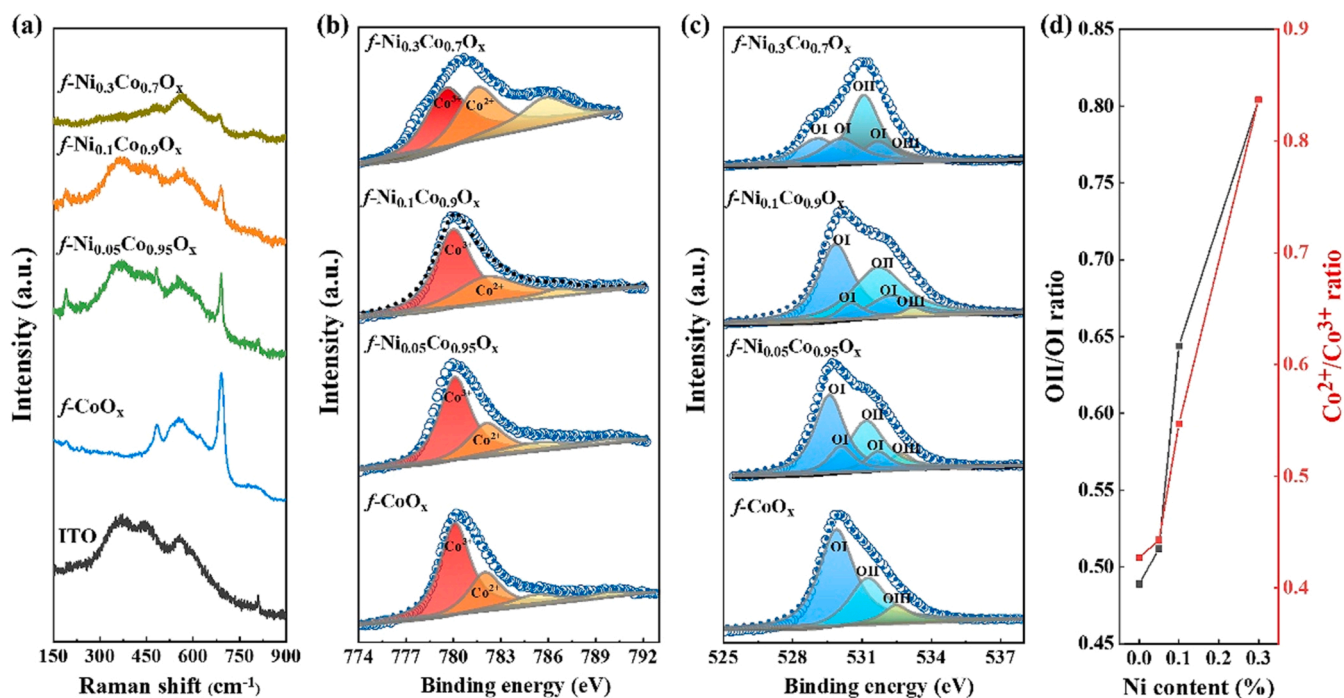

Fig. 2. (a) Raman spectra of catalyst films in dry conditions prior to OER experiment. The high-resolution XPS spectra of (b) Co $2p_{3/2}$ and (c) O1s. (d) Changes in the OII/OI ratio and Co^{2+}/Co^{3+} ratio for the samples at different Ni content in the alloy oxide.

oxide films with different Ni/Co ratios.

3.3. Applications for electrocatalytic OER and integrated photovoltaic water splitting

To demonstrate the versatility of the optically transparent f-Ni$_{0.1}$Co$_{0.9}$O$_x$, we have deposited the film on the ITO glass and 3j-a-Si photovoltaic cell to investigate its catalytic performance. The OER activity of f-Ni$_{0.1}$Co$_{0.9}$O$_x$ has been investigated by electrochemical measurements carried in O$_2$-saturated 1.0 M KOH electrolyte using a standard three electrode system calibrated with the reversible hydrogen electrode (RHE). Our results are presented the pristine data without any ohm compensation because we considered the practical application. Control samples include those synthesized with different concentrations of Ni in the NiCo alloy. Commercial RuO$_2$ is used as a benchmark sample. The linear sweep voltammetry (LSV) curves for a series of prepared samples are shown in Fig. 3a. As expected, without any iR correction, the OER overpotential (300 mV) at 10 mA cm^{-2} of f-Ni$_{0.1}$Co$_{0.9}$O$_x$ deposited on ITO glass is less than that of f-CoO$_x$ (407 mV) and commercial RuO$_2$ (380 mV), respectively. After ohm compensation (3.2 Ω), the

overpotential at 10 mA cm^{-2} of f-Ni$_{0.1}$Co$_{0.9}$O$_x$ is about 268 mV which exhibits remarkably improved current density under a constant overpotential, showing the enhanced OER activity (Fig. S10). Moreover, many kinds of conductive substrates have been used to deposit the ultrathin film indicating it is more suitable for electrode with flat surface (Fig. 3b). The overpotential is about 282 mV for f-Ni$_{0.1}$Co$_{0.9}$O$_x$ depositing on glassy carbon, which is lower than that on other substrates. It can be observed that a moderate increase of Ni in the alloy oxide facilitates OER activity but excessive Ni contents make the OER performance worse. It is definitely demonstrated that controlling Ni concentration is of importance for enhancing the activity of NiCo alloy oxides.

To deeply evaluate the OER activity, Tafel slope is fitted for f-Ni$_{0.1}$Co$_{0.9}$O$_x$ about 70.1 mV dec^{-1}, which is lower than those for f-CoO$_x$ (104.8 mV dec^{-1}) and f-NiO$_x$ (107.7 mV dec^{-1}) (Fig. 3c). This result implies a faster increase in current with potential, thus obtaining faster surface reaction kinetics on the surface of f-Ni$_{0.1}$Co$_{0.9}$O$_x$. Moreover, Fig. 3d shows the charge transfer resistance evaluated from the (Electrochemical impedance spectroscopy (EIS) measurements, which is another evidence for catalytic activity comparison. Compared with the f-CoO$_x$ and f-NiO$_x$, a smaller charge transfer resistance is observed in the f-
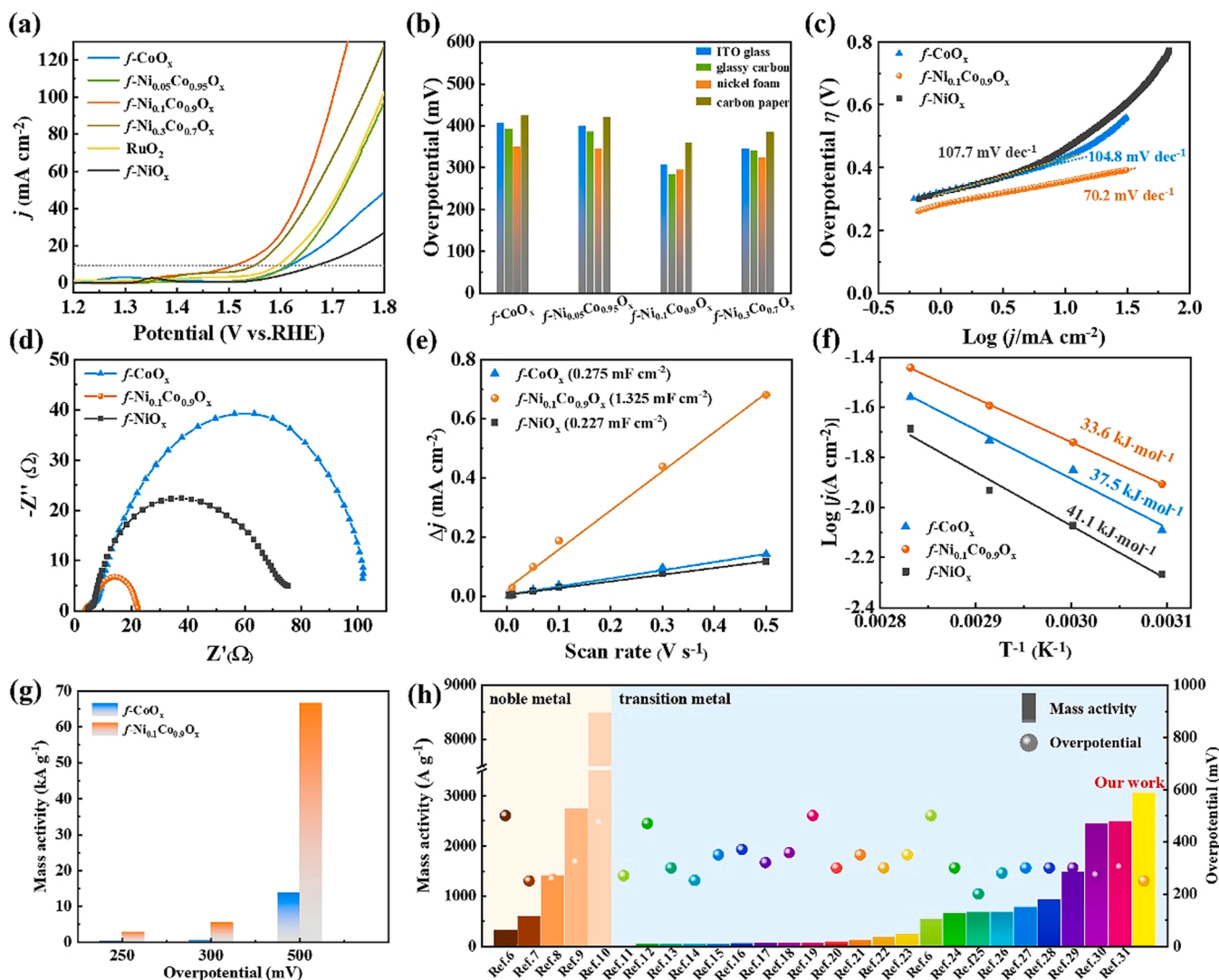

Fig. 3. Electrochemical OER performance assessments without any ohm compensation. (a) Polarization curves of Ni/Co alloy oxides. (b) Overpotential at 10 mA cm^{-2} for the different depositing substrates of the electrocatalysts. (c) Tafel plots, (d) Nyquist plots, (e) ECSA determined by double-layer-capacitance C$_{dl}$ measurements and (f) Arrhenius plots of the current at 300 mV overpotential for f-CoO$_x$, f-Ni$_{0.1}$Co$_{0.9}$O$_x$ and f-NiO$_x$, respectively. (g) The catalytic mass activity of f-CoO$_x$ and f-Ni$_{0.1}$Co$_{0.9}$O$_x$ at different overpotentials. (h) Comparison of mass activity and overpotential for f-Ni$_{0.1}$Co$_{0.9}$O$_x$ and previously reported cobalt-based and noble metal-based electrocatalysts in alkaline electrolyte from the supporting information Table S4.

$Ni_{0.1}Co_{0.9}O_x$ catalyst (Table S2 and Fig. S11), which suggests a faster charge transfer rate and lower energy barrier during OER process. Meanwhile, the number of active sites is associated with the electrochemically active surface area (ECSA). Our experiment also uses the electrochemical double layer capacitance (C_{dl}) to analyze the ECSA (Fig. 3e and Fig. S12). The ECSA of f-$Ni_{0.1}Co_{0.9}O_x$ is about 4.82 and 4.78 times that of f-CoO_x and f-NiO_x, respectively, suggesting more available active sites on the surficial structure of the f-$Ni_{0.1}Co_{0.9}O_x$. It implies that surficial oxygen vacancies and low coordination of Co can cause much more defects on the surface or the heterogeneous interface of nickel oxide/cobalt oxide, which promotes the larger ECSA of f-$Ni_{0.1}Co_{0.9}O_x$. Fig. 3f and Fig. S13 show the calculated activation energy (E_a) of 33.6 kJ mol^{-1} for f-$Ni_{0.1}Co_{0.9}O_x$, which is lower than that of f-NiO_x (41.1 kJ mol^{-1}) and f-CoO_x (37.5 kJ mol^{-1}), indicates lower activation energy barriers of OER for f-$Ni_{0.1}Co_{0.9}O_x$.

Additionally, an ultralow catalyst metal loading mass is about 1.8 µg cm^{-2} for f-$Ni_{0.1}Co_{0.9}O_x$. Among different samples tested, the outstanding mass activity of is about3055 A g^{-1} at 250 mV overpotential, almost 190 times and 7.5 times as high as f-CoO_x and commercial RuO_2 (Fig. 3g and Table S3). When applied overpotential attained 300 mV and 500 mV, the mass activity of f-$Ni_{0.1}Co_{0.9}O_x$ is about 5556 A g^{-1} and 66.7 kA g^{-1}, respectively. It is almost 11 times and 4.8 times superior to that of the f-CoO_x (Fig. 3g). Especially, the f-$Ni_{0.1}Co_{0.9}O_x$ OER catalyst outperforms virous kinds of reported transition metal compounds in KOH electrolyte (Fig. 3h, Table S4). This result indicates the alloy oxide by this simple deposition method has a sufficient atomic utilization during the OER. The stability of catalyst is all known crucial for practical application. It is noticed that f-$Ni_{0.1}Co_{0.9}O_x$ maintains its stability in catalyzing the OER reaction in long-tern water electrolysis process over 1000 cycles (Fig. S14a) and a 24-hour retention test (Fig. S14b). Furthermore, we have investigated other cobalt-based alloy oxides by this preparation method in this paper, such as FeCo and PtCo and their improved OER performance, exhibiting the advantages of binary metal catalyst (Fig. S15). This result indicates our method is a general synthesis strategy for preparing alloy oxide catalysts.

Moreover, the advantage of the e-beam evaporation alloy-UV/O_3 oxidation method is that it can be applied to any substrate and precisely controlling the thickness of the deposited film. Thus, in order to make use of the superior light transmission property of the ultrathin prepared f-$Ni_{0.1}Co_{0.9}O_x$ catalyst layer, we constructed an integrated photovoltaic system including a 3j-a-Si PV module as light absorber, f-$Ni_{0.1}Co_{0.9}O_x$ as anode catalyst and Pt wire as cathode for unassisted water splitting reaction as illustrated in Fig. 4a. The measured current of the integrated device is 8.9 mA cm^{-2} at 0 V applied bias, corresponding to a solar-to-hydrogen (STH) conversion efficiency of about 11% under 1 sun
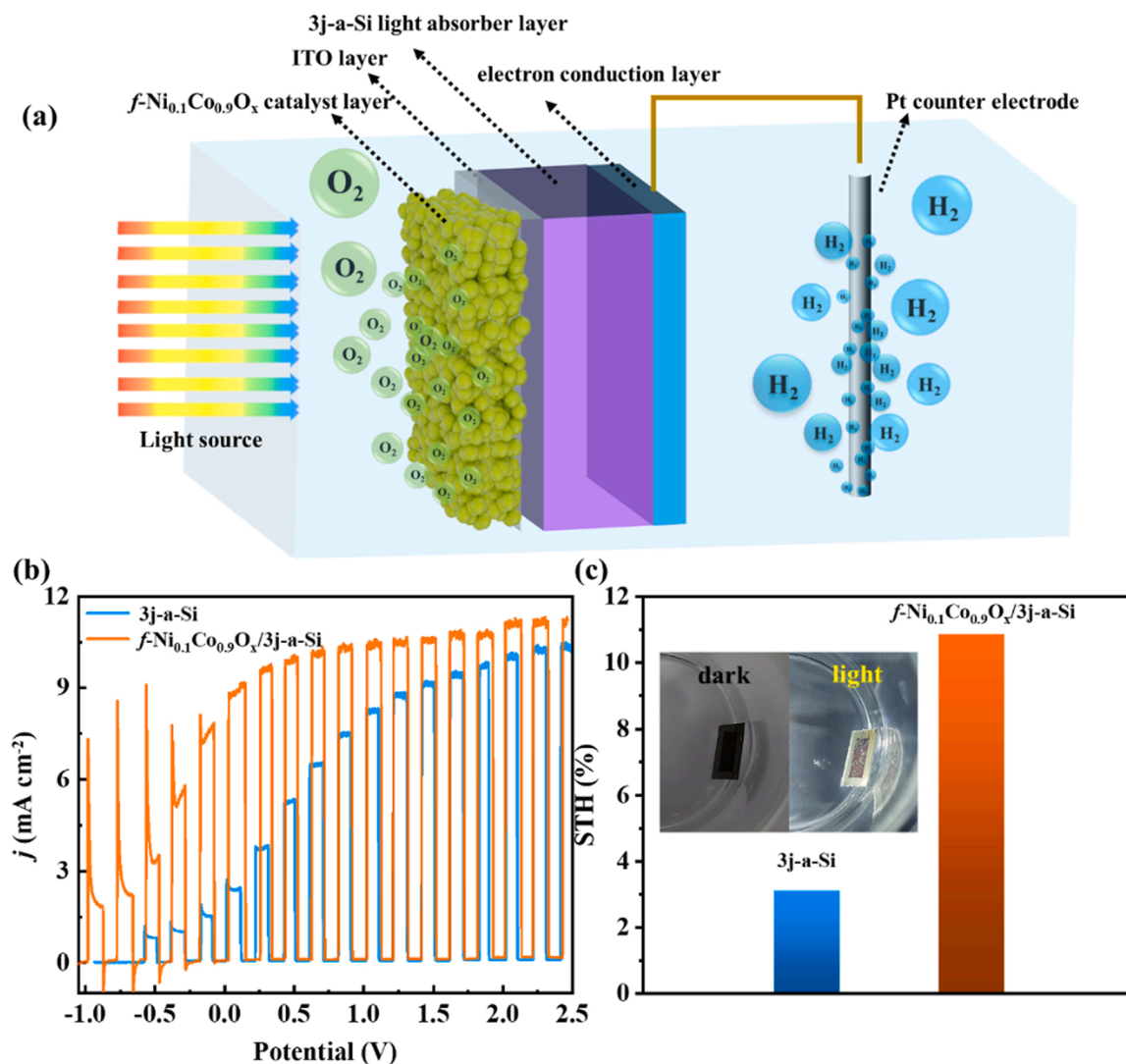

Fig. 4. (a) Schematic diagram of the integrated photovoltaic electrocatalytic water splitting system. (b) LSV curves of integrated 3j-a-Si and f-$Ni_{0.1}Co_{0.9}O_x$/3j-a-Si devices under chopped 100 ± 5 mW cm^{-2} simulated solar light. (c) STH efficiency evaluations.

illumination in 1.0 M KOH aqueous (Fig. 4b-c). Compared with pure 3j-a-Si cell, the f-Ni$_{0.1}$Co$_{0.9}$O$_x$/3j-a-Si shows about 3.5 times of the STH efficiency than that of pure 3j-a-Si, due to the high light transmission and electrocatalytic activity. Obviously can be observed, lots of H$_2$ and O$_2$ bubbles appear when irradiated by simulated-solar light (inset Fig. 4c). This application of integrated device by depositing NiCo alloy oxides on a-Si film not only for high STH efficiency but also the scaled economically beneficial systems.

Generally according to the above experimental results, it can be found Ni incorporation and oxygen vacancy are of importance for the OER performance of NiCo alloy oxides. However, it is suspicious that the real active species toward oxygen evolution and thermodynamical behavior during the reaction process for f-Ni$_{0.1}$Co$_{0.9}$O$_x$ are still not very clear only depending on the reported literatures. To this end, in situ spectra technique and simulated calculations are adopt to unravel the real electrocatalytically active species and OER mechanism in the following part.

3.4. Mechanistic insight into the surficial oxygen vacancies for OER

To directly identify the real active species and structural type prior to OER, and unrevealing the structure-activity relationship, in situ/operando Raman spectroscopy has been used to observe the surface structural variation of as-prepared NiCo alloy oxide under anodic polarization in alkaline condition (Fig. 5a) [54–56]. Observingly, for f-CoO$_x$ and f-Ni$_{0.1}$Co$_{0.9}$O$_x$, the Raman peaks are almost disappeared to be amorphous active oxides at higher anodic eletrode potential, then most intensities of Raman peaks gradually recover to the initial with the potentials decreasing to 0.1 V (vs. Hg/HgO) as shown in Fig. 5b-c. It suggests that the surface local spinel structures of these two samples are reversible [57,58]. The flexibility of surface phase is favorable for controllable stable catalytic activity, which is consistent with our experimental result about stability (Fig. S14) and also the results from Bergmann et al. [59]. Attentively, the disappearance of the Raman bands is not due to the formation of gas production, because the optical images of the sample before and after collecting each Raman spectrum are unchanged. By comparison, the A$_{1\,g}$/A$_{1\,g(E=0.1\,V)}$ Raman band ratio of f-Ni$_{0.1}$Co$_{0.9}$O$_x$ attenuates earlier than those of f-CoO$_x$ (Fig. 5d), demonstrating that the extensive distortion of the Co-O prior to OER and amorphous active species participate in the catalytic reaction at lower overpotential. The detected current density of f-Ni$_{0.1}$Co$_{0.9}$O$_x$ is higher than that of f-CoO$_x$ before OER. Based on the attenuation of A$_{1\,g}$/A$_{1\,g\,(E0=0.1\,V)}$ and higher electrochemical current density for f-Ni$_{0.1}$Co$_{0.9}$O$_x$ at lower applied potential, the decreased local spinel crystallinity and existence of more oxygen vacancies on the surface are demonstrated efficiently to promote OER activity. Additionally, it has been reported the

formation of CoO$_x$(OH)$_y$ when OER happened on the catalyst surface. The weak peak appears at 563 cm^{-1} for f-CoO$_x$ ascribing to CoO(OH) in this experiment, consisting to previous investigation [57,59]. However, this peak is not very clearly observed for f-Ni$_{0.1}$Co$_{0.9}$O$_x$ because this Raman approach lacks the surface sensitivity to detect outermost layers of the amorphourization structure [58]. In a word, in situ Raman spectra illustrates structural reversibility and oxygen vacancy-enhanced OER activity of the as-prepared alloy oxide.

Other effective evidences have been further provided for analyzing and summarizing structure-activity relationship for oxygen vacancy and OER activity. In situ UV–vis spectroelectrochemistry is used to track the pre-oxidation process of samples (Fig. S16) [60]. In order to directly compare the intrinsic catalytic properties of samples, the intensity of absorption peaks are normalized using the thickness of the samples based on the Beer's law (Fig. S17). The electrochromic phenomenon has been clearly observed during the in-situ UV–vis measurement. The darken coloration of the catalyst film can monitor the amount of oxidized Co$^{3+/4+}$. The f-Ni$_{0.1}$Co$_{0.9}$O$_x$ film darkens earlier than that of f-CoO$_x$ at earlier onset potential, indicating an increased metal redox activity (Fig. 6a-b) [61]. This result suggests Ni incorporation leading to much oxygen vacancies effectively improve water oxidation reaction using small applied potential, which is consistent with the result of Fig. 5d. The structure of f-Ni$_{0.1}$Co$_{0.9}$O$_x$ is almost unchanged comparing before and after OER test, confirming the reversible stability (Fig. S18). The cyclic voltammetry (CV) curves show that the f-Ni$_{0.1}$Co$_{0.9}$O$_x$ completes peroxide process at a relatively lower applied potential. Reversible construction also can be demonstrated by two redox couples A1/C1 and A2/C2, (A, anodic; C, cathodic), which is consistent with the operando Raman results (Fig. 6c). In addition, the electronic conductivity of the electrocatalyst plays an important role in charge transfer. The suitable oxygen vacancies and Ni incorporation optimize the conductivity of f-Ni$_{0.1}$Co$_{0.9}$O$_x$ demonstrated by small electrostatic potential (Fig. S19). This result also has been demonstrated by above EIS. Generally according to the above technique tests and OER performance results, the f-Ni$_{0.1}$Co$_{0.9}$O$_x$ with homogeneous distribution of Ni has a reversible spinel structure, much more active sites, active oxide species and enhanced electronic conductivity, thus lead to the progress of OER performance [44,62,63]. However, Fig. 6d shows excess of oxygen vacancies inhibits OER reaction. This result discloses that the precise control of oxygen vacancy concentration in the structure is responsible for the excellent OER performance. From the viewpoint of catalytic process, simulation calculation (density functional theory, DFT) further employed to disclose the essence and differences of reaction processes for f-Ni$_{0.1}$Co$_{0.9}$O$_x$ with Vos.

DFT calculations have been performed to further understand the effects of oxygen vacancy and Ni corporation. The models including
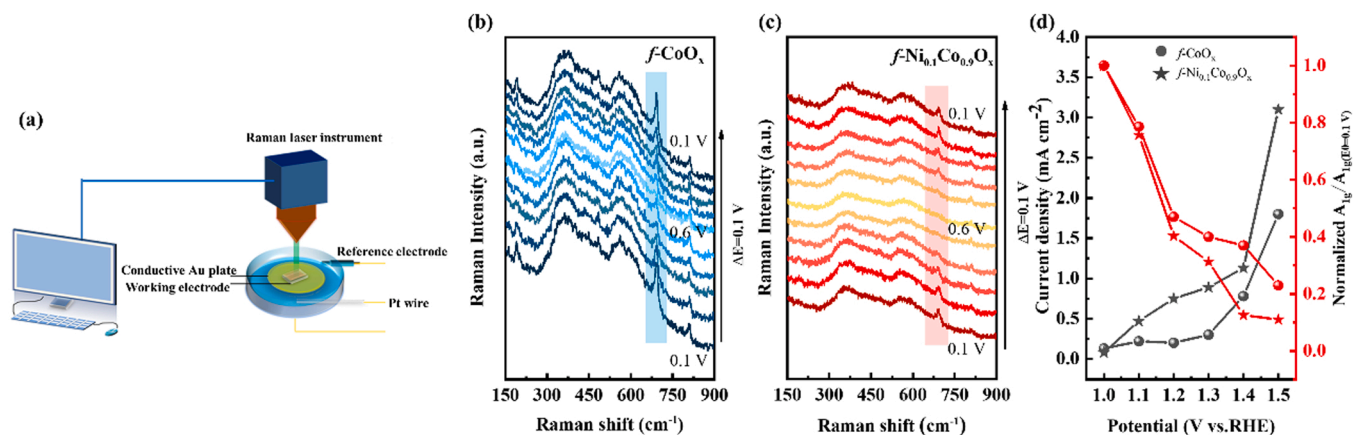

Fig. 5. (a) Illustration for the liquid cell experiment of in situ Raman spectroscopy. In situ Raman spectra of (b) f-CoO$_x$ and (c) f-Ni$_{0.1}$Co$_{0.9}$O$_x$ under different applied potentials vs. Hg/HgO (under wet conditions, 1.0 M KOH). (d) Changes in the A$_{1g}$/A$_{1g(E0=0.1V)}$ and OER current density for the samples at different applied potentials.
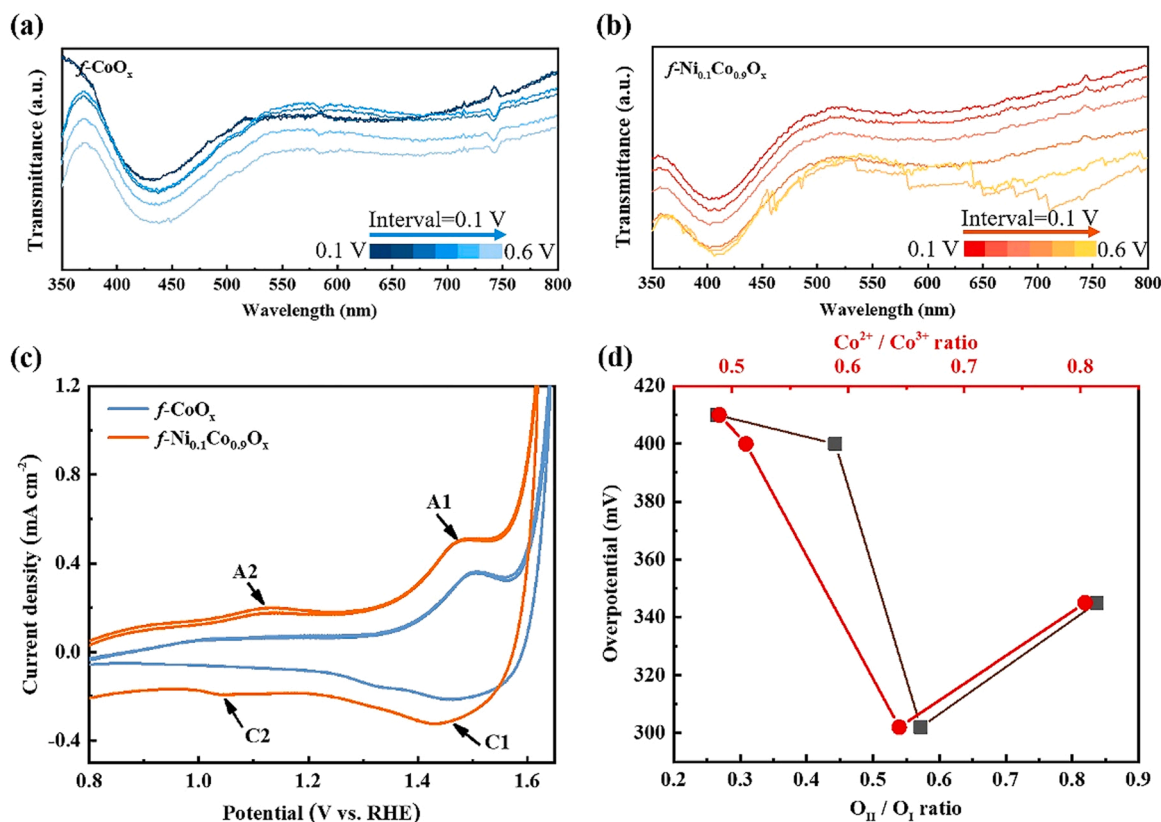
Fig. 6. In situ UV–vis spectra at different applied potentials (vs. Hg/HgO) without any iR compensation of (a) f-CoO$_x$ and (b) f-Ni$_{0.1}$Co$_{0.9}$O$_x$. (c) CV curves of samples without any iR compensation. (d) structure-activity relationship between Co^{2+}/Co^{3+}, OII/OI and overpotential (at 10 mA cm^{-2}) for f-CoO$_x$, f-Ni$_{0.05}$Co$_{0.95}$O$_x$, f-Ni$_{0.1}$Co$_{0.9}$O$_x$, and f-Ni$_{0.3}$Co$_{0.7}$O$_x$, respectively.

pristine Co$_3$O$_4$, CoO$_x$-Vo and NiCoO$_x$-Vo represent pristine Co$_3$O$_4$, f-CoO$_x$ and f-Ni$_{0.1}$Co$_{0.9}$O$_x$, respectively and the relative structure details are in the supporting information (Fig. S20). Generally, the adsorption energies of intermediate products can be computed on the basis of four-step 4e$^-$ OER mechanism to obtain the Gibbs free energy (ΔG), as a key descriptor to the activity of the electrocatalyst (in the supporting information) [38,64]. The adsorption, activation and desorption models during OER process are shown in Fig. 7a. After DFT optimization, Co^{3+} site plays as the main adsorption site for oxygenic intermediates [52, 65]. The results show that the corporation of Ni and introduction of oxygen vacancy can significantly influence the Gibbs free energy (ΔG) for intermediates formation. As shown in Fig. 7b, the ΔG2 for *OH to *O transformation shows a high value (2.10 eV), impeding the following reaction steps and resulting in a poor OER activity for pristine Co$_3$O$_4$. For CoO$_x$-Vo model, the ΔG2 is altered to be a lower value (1.45 eV), giving a relative strong binding strength with *O, thus making the transformation from *O to *OOH difficult with higher ΔG3 (1.99 eV). Compared with above models, NiCoO$_x$-Vo model exhibits a suitable value of ΔG2 (1.77 eV), also as the OER rate-determining step, which gives a moderate binding strength with *O and further facilitates the following reactions. Therefore, the above calculation results prove that Vo strengthens the adsorption of oxygenated intermediates and Ni further modulates the adsorption strength and optimizes the potential barriers. Moreover, the electronic band structures of three models are also analyzed as shown in Fig. 7c. It is clear that more electronic states appear near the Femi level for the CoO$_x$-Vo and NiCoO$_x$-Vo models, which can lead to the high electrical conductivity [27]. Furthermore, the D-band centers of the Co atoms have been calculated which often used as the describer to demonstrate the binding strength of the adsorbates on catalyst surface [23]. It is found that the D-band center of Co in the structure of NiCoO$_x$-Vo model is below the Fermi level with a lower

energy (-3.10 eV) than that of CoO$_x$-Vo (-3.01 eV) and pristine Co$_3$O$_4$ model (-2.78 eV). It is known that for transition metal-based catalysts, the adsorbate interacts with D-electrons giving rise to bonding and antibonding orbitals. The higher the center of D-band is, the higher the antibonding states, resulting in a stronger adsorption, which inhibits reaction kinetics. Therefore, these demonstrations further indicates that the Co atoms near the Vo and Ni with a lower D-band center possess suitable adsorption for oxygen species and thus enhance the OER catalytic activity. Additionally, the Bader charge analysis of Co^{3+} active site and partial charge distribution of these three models are shown in Fig. S21 and Table S5, which demonstrate Ni atom and oxygen vacancy increase the degree of the delocalization of the electron cloud of the pristine O situation and density of state around Co^{3+} to result in a facial charge transfer for OER process.

On the whole, the improved OER activity can be attributed to the following aspects. Firstly, regulating the oxygen vacancy concentration by changing Ni/Co proportion in the alloy facilitates more active sites on the surface and edge in the defective spinel structure. Secondly, the under-coordinated Ni—O and Co—O bonds introduce oxygen vacancies contributing to more unsaturated electronic configurations at the catalyst/reactants interface, thus easily forming intermediates or absorbents to speed up the reaction kinetics. Also, suitable proportion of the oxygen vacancies optimizes the material conductivity for fast charge transfer. Thirdly, the reversible structural flexibility of the active species for f-Ni$_{0.1}$Co$_{0.9}$O$_x$ enables the stable existence of electrocatalyst before and after OER, which is meaningful for hundreds of using cycles for the commercial application of energy storage. Last but not the least, the controlled thin thickness and low-loading of catalyst benefits the high mass activity of OER, which can reduce the production cost. Moreover, the usage of the appropriate thickness of f-Ni$_{0.1}$Co$_{0.9}$O$_x$ is also important for high STH efficiency for integrated photovoltaic electrocatalysis
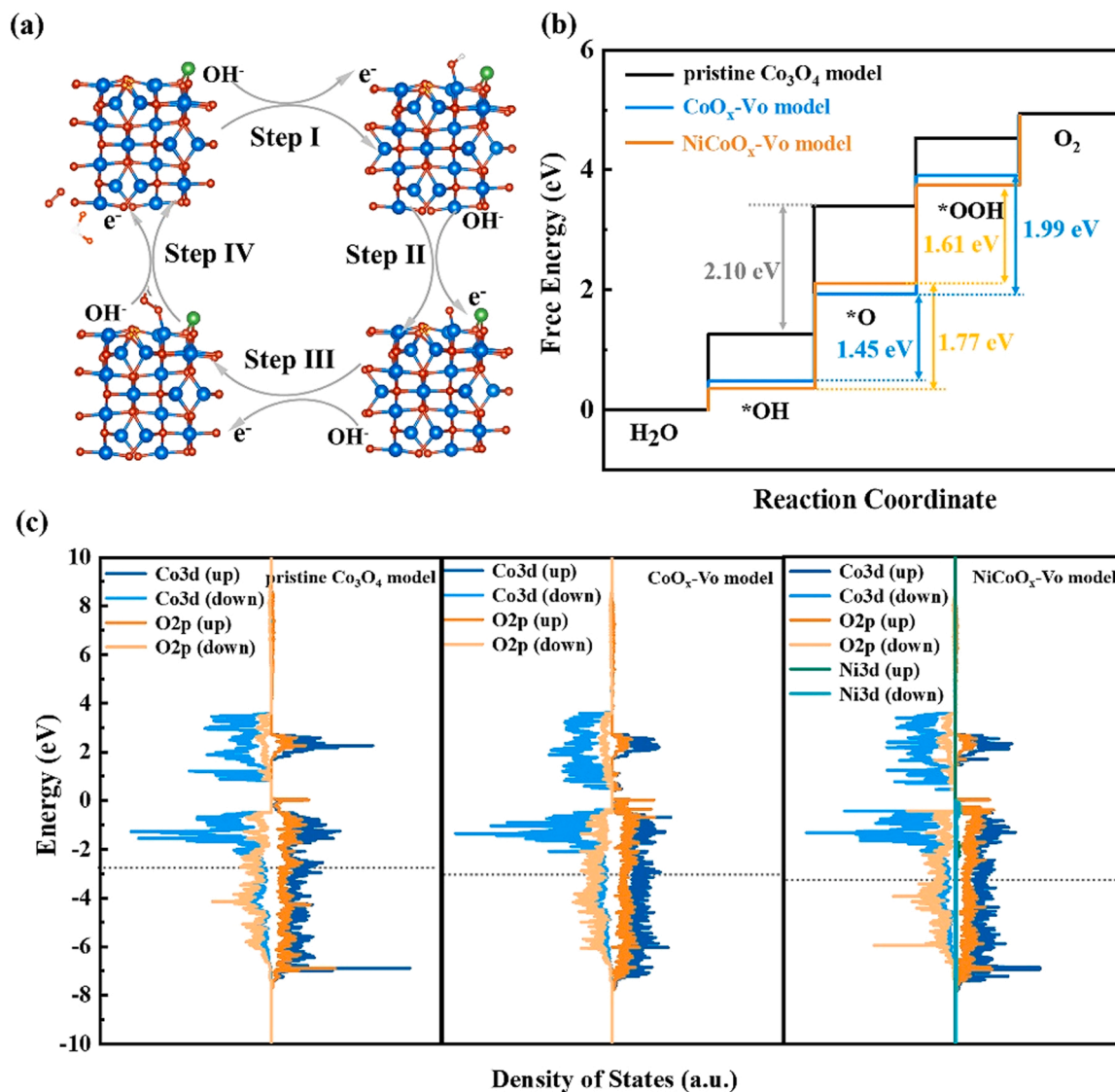
Fig. 7. (a) Proposed 4e⁻ pathways with *OH, *O, and *OOH intermediates of OER on NiCoO$_x$-Vo model (The yellow circle presents the position of the O vacancy; red O, white H, blue Co and green Ni). (b) Calculated free energy diagram of OER intermediates at zero potential (U = 0). (c) The diagram of PDOS (projected densities of states) and D-band centers (dotted lines). (For interpretation of the references to colour in this figure, the reader is referred to the web version of this article.)

system.

4. Conclusions

In summary, the optical transparent NiCo alloy oxide electrocatalyst has been successfully synthesized by e-beam evaporation alloy-UV/O$_3$ oxidation method. The obtained ultrathin f-Ni$_{0.1}$Co$_{0.9}$O$_x$ exhibits excellent OER performance, offering 3055 A g^{-1} mass activity at 250 mV overpotential almost 190 times and 7.5 times as much high as commercial RuO$_2$ and f-CoO$_x$, respectively. It has been revealed that the enhanced catalytic activity is mainly related to the controllable oxygen vacancy concentration, ultrahigh atomic utilization and stably reversible structure. Based on the observation of such structural transformation using in situ Raman spectroscopy, the fast pre-oxidation process and chemical structure reversibility of f-Ni$_{0.1}$Co$_{0.9}$O$_x$ occurred on the surface have been demonstrated for high OER activity and stability. DFT calculations unveil that the modification of electronic structure by changing the metal-oxygen coordination and Vo facilitate charge transfer and a decreased adsorption energy barrier for the high catalytic performance. This work not only provides strategy to modulate Vos of various multi-composition alloy oxides electrocatalysts by a bimetal co-evaporation-UV/O$_3$ oxidization, but also offers a large-scale production of the electrocatalyst applying for solar-chemical energy conversion and storage.

Acknowledgements

Appendix A. Supporting information

Supplementary data associated with this article can be found in the online version at doi:10.1016/j.apcatb.2022.121301.

References

[1] J. Hou, Y. Wu, B. Zhang, S. Cao, Z. Li, L. Sun, Rational design of nanoarray architectures for electrocatalytic water splitting, Adv. Funct. Mater. 29 (2019), 1808367, https://doi.org/10.1002/adfm.201808367.

[2] L. Han, S. Dong, E. Wang, Transition-metal (Co, Ni, and Fe)-based electrocatalysts for the water oxidation reaction, Adv. Mater. 28 (2016) 9266–9291, https://doi.org/10.1002/adma.201602270.

[3] N.-T. Suen, S.-F. Hung, Q. Quan, N. Zhang, Y.-J. Xu, H.M. Chen, Electrocatalysis for the oxygen evolution reaction: recent development and future perspectives, Chem. Soc. Rev. 46 (2017) 337–365, https://doi.org/10.1039/c6cs00328a.

[4] J. Song, Z.-F. Huang, L. Pan, K. Li, X. Zhang, L. Wang, J.-J. Zou, Review on selective hydrogenation of nitroarene by catalytic, photocatalytic and electrocatalytic reactions, Appl. Catal. B Environ. 227 (2018) 386–408, https://doi.org/10.1016/j.apcatb.2018.01.052.

[5] G. Buvat, M.J. Eslamibidgoli, A.H. Youssef, S. Garbarino, A. Ruediger, M. Eikerling, D. Guay, Effect of IrO₆ octahedron distortion on the OER activity at (100) IrO₂ thin film, ACS Catal. 10 (2020) 806–817, https://doi.org/10.1021/acscatal.9b04347.

[6] E. Antolini, Iridium as catalyst and cocatalyst for oxygen evolution/reduction in acidic polymer electrolyte membrane electrolyzers and fuel cells, ACS Catal. 4 (2014) 1426–1440, https://doi.org/10.1021/cs4011875.

[7] S. Cherevko, S. Geiger, O. Kasian, N. Kulyk, J.-P. Grote, A. Savan, B.R. Shrestha, S. Merzlikin, B. Breitbach, A. Ludwig, K.J.J. Mayrhofer, Oxygen and hydrogen evolution reactions on Ru, RuO₂, Ir, and IrO₂ thin film electrodes in acidic and alkaline electrolytes: a comparative study on activity and stability, Catal. Today 262 (2016) 170–180, https://doi.org/10.1016/j.cattod.2015.08.014.

[8] F. Song, L. Bai, A. Moysiadou, S. Lee, C. Hu, L. Liardet, X. Hu, Transition metal oxides as electrocatalysts for the oxygen evolution reaction in alkaline solutions: an application-inspired renaissance, J. Am. Chem. Soc. 140 (2018) 7748–7759, https://doi.org/10.1021/jacs.8b04546.

[9] R.D.L. Smith, M.S. Prevot, R.D. Fagan, Z. Zhang, P.A. Sedach, M.K.J. Siu, S. Trudel, C.P. Berlinguette, Photochemical route for accessing amorphous metal oxide materials for water oxidation catalysis, Science 340 (2013) 60–63, https://doi.org/10.1126/science.1233638.

[10] X. Liu, M. Park, M.G. Kim, S. Gupta, G. Wu, J. Cho, Integrating NiCo alloys with their oxides as efficient bifunctional cathode catalysts for rechargeable zinc–air batteries, Angew. Chem. Int. Ed. 54 (2015) 9654–9658, https://doi.org/10.1002/anie.201503612.

[11] C. Wang, L.-L. Gu, S.-Y. Qiu, J. Gao, Y.-C. Zhang, K.-X. Wang, J.-J. Zou, P.-J. Zuo, X.-D. Zhu, Modulating CoFe₂O₄ nanocube with oxygen vacancy and carbon wrapper towards enhanced electrocatalytic nitrogen reduction to ammonia, Appl. Catal. B Environ. 297 (2021) 120452, https://doi.org/10.1016/j.apcatb.2021.120452.

[12] C.G. Morales-Guio, L. Liardet, X. Hu, Oxidatively electrodeposited thin-film transition metal (Oxy)hydroxides as oxygen evolution catalysts, J. Am. Chem. Soc. 138 (2016) 8946–8957, https://doi.org/10.1021/jacs.6b05196.

[13] M.A. Sayeed, T. Herd, A.P. O'Mullane, Direct electrochemical formation of nanostructured amorphous Co(OH)₂ on gold electrodes with enhanced activity for the oxygen evolution reaction, J. Mater. Chem. A 4 (2015) 991–999, https://doi.org/10.1039/c5ta09125j.

[14] J. Wang, W. Cui, Q. Liu, Z. Xing, A.M. Asiri, X. Sun, Recent progress in cobalt-based heterogeneous catalysts for electrochemical water splitting, Adv. Mater. 28 (2016) 215–230, https://doi.org/10.1002/adma.201502696.

[15] H. Zeng, Mh Oubla, X. Zhong, N. Alonso-Vante, F. Du, Y. Xie, Y. Huang, J. Ma, Rational defect and anion chemistries in Co₃O₄ for enhanced oxygen evolution reaction, Appl. Catal. B Environ. 281 (2021), 119535, https://doi.org/10.1016/j.apcatb.2020.119535.

[16] J. Liu, C. Wang, H. Sun, H. Wang, F. Rong, L. He, Y. Lou, S. Zhang, Z. Zhang, M. Du, CoOₓ/CoNᵧ nanoparticles encapsulated carbon-nitride nanosheets as an efficiently trifunctional electrocatalyst for overall water splitting and Zn-air battery, Appl. Catal. B Environ. 279 (2020) 119407, https://doi.org/10.1016/j.apcatb.2020.119407.

[17] Y. Duan, Z.-Y. Yu, S.-J. Hu, X.-S. Zheng, C.-T. Zhang, H.-H. Ding, B.-C. Hu, Q.-Q. Fu, Z.-L. Yu, X. Zheng, J.-F. Zhu, M.-R. Gao, S.-H. Yu, Scaled-up synthesis of amorphous NiFeMo oxides and their rapid surface reconstruction for superior oxygen evolution catalysis, Angew. Chem. Int. Ed. 58 (2019) 15772–15777, https://doi.org/10.1002/anie.201909939.

[18] Y.K. Kim, J.H. Kim, Y.H. Jo, J.S. Lee, Precipitating metal nitrate deposition of amorphous metal oxyhydroxide electrodes containing Ni, Fe, and Co for electrocatalytic water oxidation, ACS Catal. 9 (2019) 9650–9662, https://doi.org/10.1021/acscatal.9b02701.

[19] D. Yan, Y. Li, J. Huo, R. Chen, L. Dai, S. Wang, Defect chemistry of nonprecious-metal electrocatalysts for oxygen reactions, Adv. Mater. 29 (2017), 1606459, https://doi.org/10.1002/adma.201606459.

[20] C. Meng, M. Lin, X. Sun, X. Chen, X. Chen, X. Du, Y. Zhou, Laser synthesis of oxygen vacancy-modified CoOOH for highly efficient oxygen evolution, Chem. Commun. 55 (2019) 2904–2907, https://doi.org/10.1039/c8cc08951e.

[21] S. Yang, Y. Liu, Y. Hao, X. Yang, W.A. Goddard Iii, X.L. Zhang, B. Cao, Oxygen-vacancy abundant ultrafine Co₃O₄/graphene composites for high-rate supercapacitor electrodes, Adv. Sci. 5 (2018), 1700659, https://doi.org/10.1002/advs.201700659.

[22] X. Liu, L. Zhang, Y. Zheng, Z. Guo, Y. Zhu, H. Chen, F. Li, P. Liu, B. Yu, X. Wang, J. Liu, Y. Chen, M. Liu, Uncovering the effect of lattice strain and oxygen deficiency on electrocatalytic activity of perovskite cobaltite thin films, Adv. Sci. 6 (2019), 1801898, https://doi.org/10.1002/advs.201801898.

[23] D. He, X. Song, W. Li, C. Tang, J. Liu, Z. Ke, C. Jiang, X. Xiao, Active electron density modulation of Co₃O₄-based catalysts enhances their oxygen evolution performance, Angew. Chem. Int. Ed. 59 (2020) 6929–6935, https://doi.org/10.1002/anie.202001681.

[24] B. Jia, R. Hao, Z. Huang, P. Hu, L. Li, Y. Zhang, L. Guo, Creating ultrathin amorphous metal hydroxide and oxide nanosheet libraries, J. Mater. Chem. A 7 (2019) 4383–4388, https://doi.org/10.1039/c8ta11525g.

[25] X. Chen, T. Huang, D.-H. Kuo, H. Sun, H. Li, O.A. Zelekew, A.B. Abdeta, Q. Wu, J. Zhang, Z. Yuan, J. Lin, Material design with the concept of solid solution-type defect engineering in realizing the conversion of an electrocatalyst of NiS₂ into a photocatalyst for hydrogen evolution, Appl. Catal. B Environ. 298 (2021), 120542, https://doi.org/10.1016/j.apcatb.2021.120542.

[26] Z. Li, Y. Zhang, Y. Feng, Ci Cheng, Xe Du, Co₃O₄ nanoparticles with ultrasmall size and abundant oxygen vacancies for boosting oxygen involved reactions, Adv. Funct. Mater. 29 (2019), 2000364, https://doi.org/10.1002/adfm.202000364.

[27] T. Zhang, M.-Y. Wu, D.-Y. Yan, J. Mao, H. Liu, W.-B. Hu, X.-W. Du, T. Ling, S.-Z. Qiao, Engineering oxygen vacancy on NiO nanorod arrays for alkaline hydrogen evolution, Nano Energy 43 (2018) 103–109, https://doi.org/10.1016/j.nanoen.2017.11.015.

[28] G. Song, R. Gao, Z. Zhao, Y. Zhang, H. Tan, H. Li, D. Wang, Z. Sun, M. Feng, High-spin state Fe(III) doped TiO₂ for electrocatalytic nitrogen fixation induced by surface F modification, Appl. Catal. B Environ. 301 (2022), 120809, https://doi.org/10.1016/j.apcatb.2021.120809.

[29] S. Liu, H. Cheng, K. Xu, H. Ding, J. Zhou, B. Liu, W. Chu, C. Wu, Y. Xie, Dual modulation via electrochemical reduction activiation on electrocatalysts for enhanced oxygen evolution reaction, ACS Energy Lett. 4 (2019) 423–429, https://doi.org/10.1021/acsenergylett.8b01974.

[30] Z. Xiao, Y. Wang, Y.-C. Huang, Z. Wei, C.-L. Dong, J. Ma, S. Shen, Y. Li, S. Wang, Filling the oxygen vacancies in Co₃O₄ with phosphorus: an ultra-efficient electrocatalyst for overall water splitting, Energ. Environ. Sci. 10 (2017) 2563–2569, https://doi.org/10.1039/c7ee01917c.

[31] Y. Zhu, L. Zhang, B. Zhao, H. Chen, X. Liu, R. Zhao, X. Wang, J. Liu, Y. Chen, M. Liu, Improving the activity for oxygen evolution reaction by tailoring oxygen defects in double perovskite oxides, Adv. Funct. Mater. 29 (2019), 1901783, https://doi.org/10.1002/adfm.201901783.

[32] B.-J. Kim, E. Fabbri, D.F. Abbott, X. Cheng, A.H. Clark, M. Nachtegaal, M. Borlaf, I.E. Castelli, T. Graule, T.J. Schmidt, Functional role of fe-doping in co-based perovskite oxide catalysts for oxygen evolution reaction, J. Am. Chem. Soc. 141 (2019) 5231–5240, https://doi.org/10.1021/jacs.8b12101.

[33] J. Yin, J. Jin, H. Liu, B. Huang, M. Lu, J. Li, H. Liu, H. Zhang, Y. Peng, P. Xi, C.-H. Yan, NiCo₂O₄-based nanosheets with uniform 4 nm mesopores for excellent Zn–air battery performance, Adv. Mater. 32 (2020), 2001651, https://doi.org/10.1002/adma.202001651.

[34] J. Zhang, J. Qian, J. Ran, P. Xi, L. Yang, D. Gao, Engineering lower coordination atoms onto NiO/Co₃O₄ heterointerfaces for boosting oxygen evolution reactions, ACS Catal. 10 (2020) 12376–12384, https://doi.org/10.1021/acscatal.0c03491.

[35] Y. Yao, Z. Huang, P. Xie, S.D. Lacey, R.J. Jacob, H. Xie, F. Chen, A. Nie, T. Pu, M. Rehwoldt, Carbothermal shock synthesis of high-entropy-alloy nanoparticles, Science 359 (2018) 1489–1494, https://doi.org/10.1126/science.aan5412.

[36] M. Wu, M. Cui, L. Wu, S. Hwang, C. Yang, Q. Xia, G. Zhong, H. Qiao, W. Gan, X. Wang, D. Kline, M.R. Zachariah, D. Su, T. Li, L. Hu, Hierarchical polyelemental nanoparticles as bifunctional catalysts for oxygen evolution and reduction reactions, Adv. Energy Mater. 10 (2020), 2001119, https://doi.org/10.1002/aenm.202001119.

[37] R. Islam, G. Chen, P. Ramesh, J. Suh, K.C. Saraswat, Investigation of the changes in electronic properties of nickel oxide (NiOₓ) Due to UV/Ozone treatment, Acs Appl. Mater. Inter. 9 (2017) 17201–17207, https://doi.org/10.1021/acsami.7b01629.

[38] Y. Zhu, L. Zhang, B. Zhao, H. Chen, M. Liu, Improving the activity for oxygen evolution reaction by tailoring oxygen defects in double perovskite oxides, Adv. Funct. Mater. 29 (2019), 1901783, https://doi.org/10.1002/adfm.201901783.

[39] K. Sun, I.A. Moreno-Hernandez, W.C. Schmidt, X. Zhou, J.C. Crompton, R. Liu, F.H. Saadi, Y. Chen, K.M. Papadantonakis, N.S. Lewis, A comparison of the chemical, optical and electrocatalytic properties of water-oxidation catalysts for use in integrated solar-fuel generators, Energ. Environ. Sci. 10 (2017) 987–1002, https://doi.org/10.1039/c6ee03563a.

[40] Q. Zhang, Z.D. Wei, C. Liu, X. Liu, X.Q. Qi, S.G. Chen, W. Ding, Y. Ma, F. Shi, Y.M. Zhou, Copper-doped cobalt oxide electrodes for oxygen evolution reaction prepared by magnetron sputtering, Int. J. Hydrog. Energy 37 (2012) 822–830, https://doi.org/10.1016/j.ijhydene.2011.04.051.

[41] C. Xiao, X. Lu, C. Zhao, Unusual synergistic effects upon incorporation of Fe and/or Ni into mesoporous Co₃O₄ for enhanced oxygen evolution, Chem. Commun. 50 (2014) 10122–10125, https://doi.org/10.1039/c4cc04922e.

[42] B. Rivas-Murias, V. Salgueiriño, Thermodynamic CoO–Co_3O_4 crossover using Raman spectroscopy in magnetic octahedron-shaped nanocrystals, J. Raman Spectrosc. 48 (2017) 837–841, https://doi.org/10.1002/jrs.5129.

[43] T.N. Lambert, J.A. Vigil, S.E. White, D.J. Davis, S.J. Limmer, P.D. Burton, E. N. Coker, T.E. Beechem, M.T. Brumbach, Electrodeposited $Ni_xCo_{3-x}O_4$ nanostructured films as bifunctional oxygen electrocatalysts, Chem. Commun. 51 (2015) 9511–9514, https://doi.org/10.1039/c5cc02262b.

[44] Z. Chen, L. Cai, X. Yang, C. Kronawitter, L. Guo, S. Shen, B.E. Koel, Reversible structural evolution of $NiCoO_xH_y$ during the oxygen evolution reaction and identification of the catalytically active phase, ACS Catal. 8 (2018) 1238–1247, https://doi.org/10.1039/c5cc02262b.

[45] Z. Li, Y. Zhang, Y. Feng, C.-Q. Cheng, X.-W. Du, Co_3O_4 nanoparticles with ultrasmall size and abundant oxygen vacancies for boosting oxygen involved reactions, Adv. Funct. Mater. 30 (2020), 2000364, https://doi.org/10.1002/adfm.202000364.

[46] J. Wang, R. Gao, D. Zhou, Z. Chen, Z. Wu, G. Schumacher, Z. Hu, X. Liu, Boosting the electrocatalytic activity of Co_3O_4 nanosheets for a Li-O_2 battery through modulating inner oxygen vacancy and exterior Co^{3+}/Co^{2+} ratio, ACS Catal. 7 (2017) 6533–6541, https://doi.org/10.1021/acscatal.7b02313.

[47] X. Han, G. He, Y. He, J. Zhang, X. Zheng, L. Li, C. Zhong, W. Hu, Y. Deng, T.-Y. Ma, Engineering catalytic active sites on cobalt oxide surface for enhanced oxygen electrocatalysis, Adv. Energy Mater. 8 (2018), 1702222, https://doi.org/10.1002/aenm.201702222.

[48] M.C. Biesinger, B.P. Payne, A.P. Grosvenor, L.W.M. Lau, A.R. Gerson, R.S.C. Smart, Resolving surface chemical states in xps analysis of first row transition metals, oxides and hydroxides: Cr, Mn, Fe, Co and Ni, Appl. Surf. Sci. 257 (2011) 2717–2730, https://doi.org/10.1016/j.apsusc.2010.07.086.

[49] Y. Li, Z.-S. Wu, P. Lu, X. Wang, W. Liu, Z. Liu, J. Ma, W. Ren, Z. Jiang, X. Bao, High-valence nickel single-atom catalysts coordinated to oxygen sites for extraordinarily activating oxygen evolution reaction, Adv. Sci. 7 (2020), 1903089, https://doi.org/10.1002/advs.201903089.

[50] L. Zhang, C. Lu, F. Ye, Z. Wu, Y. Wang, L. Jiang, L. Zhang, C. Cheng, Z. Sun, L. Hu, Vacancies boosting strategy enabling enhanced oxygen evolution activity in a library of novel amorphous selenite electrocatalysts, Appl. Catal. B Environ. 284 (2021), 119758, https://doi.org/10.1016/j.apcatb.2020.119758.

[51] G. Cheng, T. Kou, J. Zhang, C. Si, H. Gao, Z. Zhang, $O_2{}^{2-}/O^-$ Functionalized oxygen-deficient Co_3O_4 nanorods as high performance supercapacitor electrodes and electrocatalysts towards water splitting, Nano Energy 38 (2017) 155–166, https://doi.org/10.1016/j.nanoen.2017.05.043.

[52] Z. Shao, J. Sun, N. Guo, F. He, K. Huang, F. Tian, Q. Wang, Boosting electrocatalysis by heteroatom doping and oxygen vacancies in hierarchical ni-co based nitride phosphide hybrid, J. Power Sources 422 (2019) 33–41, https://doi.org/10.1016/j.jpowsour.2019.03.036.

[53] S. Yang, Y. Liu, Y. Hao, X. Yang, B. Cao, Oxygen-vacancy abundant ultrafine Co_3O_4/graphene composites for high-rate supercapacitor electrodes, Adv. Sci. 5 (2018), 1700659, https://doi.org/10.1002/advs.201700659.

[54] X. Li, H.-Y. Wang, H. Yang, W. Cai, S. Liu, B. Liu, In situ/operando characterization techniques to probe the electrochemical reactions for energy conversion, Small Methods 2 (2018), 1700395, https://doi.org/10.1002/smtd.201700395.

[55] K. Zhu, X. Zhu, W. Yang, Application of in situ techniques for the characterization of nife-based oxygen evolution reaction (OER) electrocatalysts, Angew. Chem. Int. Ed. 58 (2019) 1252–1265, https://doi.org/10.1002/anie.201802923.

[56] A. Mavrič, M. Fanetti, Y. Lin, M. Valant, C. Cui, Spectroelectrochemical tracking of nickel hydroxide reveals its irreversible redox states upon operation at high current density, ACS Catal. 10 (2020) 9451–9457, https://doi.org/10.1021/acscatal.0c01813.

[57] B.S. Yeo, A.T. Bell, Enhanced activity of gold-supported cobalt oxide for the electrochemical evolution of oxygen, J. Am. Chem. Soc. 133 (2011) 5587–5593, https://doi.org/10.1021/ja200559j.

[58] Z. Chen, L. Cai, X. Yang, C. Kronawitter, L. Guo, S. Shen, B.E. Koel, Reversible structural evolution of $NiCoO_xH_y$ during the oxygen evolution reaction and identification of the catalytically active phase, ACS Catal. 8 (2018) 1238–1247, https://doi.org/10.1021/acscatal.7b03191.

[59] A. Bergmann, E. Martinez-Moreno, D. Teschner, P. Chernev, M. Gliech, J.F. De Araújo, T. Reier, H. Dau, P. Strasser, Reversible amorphization and the catalytically active state of crystalline Co_3O_4 during oxygen evolution, Nat. Commun. 6 (2015) 8625, https://doi.org/10.1038/ncomms9625.

[60] M. Görlin, J. Ferreira de Araújo, H. Schmies, D. Bernsmeier, S. Dresp, M. Gliech, Z. Jusys, P. Chernev, R. Kraehnert, H. Dau, P. Strasser, Tracking catalyst redox states and reaction dynamics in Ni–Fe oxyhydroxide oxygen evolution reaction electrocatalysts: the role of catalyst support and electrolyte pH, J. Am. Chem. Soc. 139 (2017) 2070–2082, https://doi.org/10.1021/jacs.6b12250.

[61] Z. Goldsmith, A. Harshan, J. Gerken, M. Vörös, G. Galli, S. Stahl, S. Hammes-Schiffer, Characterization of NiFe oxyhydroxide electrocatalysts by integrated electronic structure calculations and spectroelectrochemistry, PNAS 114 (2017), 201702081, https://doi.org/10.1073/pnas.1702081114.

[62] R. Zhang, Y.-C. Zhang, L. Pan, G.-Q. Shen, N. Mahmood, Y.-H. Ma, Y. Shi, W. Jia, L. Wang, X. Zhang, W. Xu, J.-J. Zou, Engineering cobalt defects in cobalt oxide for highly efficient electrocatalytic oxygen evolution, ACS Catal. 8 (2018) 3803–3811, https://doi.org/10.1021/acscatal.8b01046.

[63] Y. Li, F.-M. Li, X.-Y. Meng, S.-N. Li, J.-H. Zeng, Y. Chen, Ultrathin Co_3O_4 nanomeshes for the oxygen evolution reaction, ACS Catal. 8 (2018) 1913–1920, https://doi.org/10.1021/acscatal.7b03949.

[64] Y.-R. Hong, S. Mhin, K.-M. Kim, W.-S. Han, H. Choi, G. Ali, K.Y. Chung, H.J. Lee, S.-I. Moon, S. Dutta, S. Sun, Y.-G. Jung, T. Song, H. Han, Electrochemically activated cobalt nickel sulfide for an efficient oxygen evolution reaction: partial amorphization and phase control, J. Mater. Chem. A 7 (2019) 3592–3602, https://doi.org/10.1039/c8ta10142f.

[65] M. Tahir, L. Pan, R. Zhang, Y.-C. Wang, G. Shen, I. Aslam, M.A. Qadeer, N. Mahmood, W. Xu, L. Wang, X. Zhang, J.-J. Zou, High-valence-state NiO/Co_3O_4 nanoparticles on nitrogen-doped carbon for oxygen evolution at low overpotential, ACS Energy Lett. 2 (2017) 2177–2182, https://doi.org/10.1021/acsenergylett.7b00691.